


Carrier-induced metal-insulator transition in trirutile MgTa_2O_6 Kyle D. Miller^{*} and James M. Rondinelli[†]*Department of Materials Science and Engineering, Northwestern University, Evanston, Illinois 60208, USA* (Received 21 April 2022; accepted 5 July 2022; published 21 July 2022)

Materials exhibiting metal-insulator transitions (MITs) are proposed platforms for next-generation low-power electronics. Many of these materials exhibit strong coupling between the electronic and lattice degrees of freedom, which makes them ideal systems to examine the interplay between lattice dynamics, electronic structure, and magnetic order. The rutile structure, featuring edge-connected octahedral chains along its c axis, permits metal-metal interactions that can induce metal-insulator transitions. Although the MITs in rutile-structured compounds have been thoroughly studied, the derivative trirutile phase, which accommodates similar metal-metal interactions, has yet to be examined in the context of MITs. Here we use density functional theory calculations to investigate a carrier-driven MIT in trirutile MgTa_2O_6 , a d^0 insulator with a suitable axial ratio. Our calculations suggest the existence of four distinct phases in MgTa_2O_6 with increasing electron concentration: nonmagnetic insulator, ferromagnetic (FM) metal, FM half-metal, and nonmagnetic insulator. We explain how the resulting electronic phases arise from changes in atomic structure with increasing carrier density. Our results indicate that trirutile oxides may be a promising materials class for which to access and functionalize MITs.

DOI: [10.1103/PhysRevMaterials.6.075007](https://doi.org/10.1103/PhysRevMaterials.6.075007)

I. INTRODUCTION

Materials hosting strongly correlated electrons remain of immense interest owing both to persistent difficulty in modeling their electronic structures and describing their related phenomena, such as metal-insulator transitions (MITs) [1,2], superconductivity [3,4], and colossal magnetoresistance [5], used in engineered systems. The resistive switching behavior present in MIT materials has a broad range of applications in microelectronics [6]. Beyond the Mott-based transistor [7–9], recent work highlights potential utility of the MIT in VO_2 as a photodetector [10] and as a neuromorphic circuit element [11].

In addition to electron-electron interactions, some MITs are facilitated by changes in crystal symmetry. Given these two driving forces, we can describe four relevant classes of insulators: charge-transfer, Mott, Peierls, and Mott-Peierls. Charge-transfer insulators are governed by Coulombic repulsion between p and d orbitals, yielding a p - d energy gap. Mott, or Mott-Hubbard, insulators are also governed by Coulombic repulsion but between two d orbitals in neighboring unit cells, yielding a d - d gap. Peierls insulators possess a gap formed via symmetry breaking (often manifesting as metal-metal dimerization), which stabilizes the crystal by splitting a partially filled band into two bands, one stabilized and filled and the other destabilized and empty. Mott-Peierls insulators feature a combination of Coulombic and symmetry-breaking forces. All insulators in these classes can be metallized, so-called carrier-induced MITs, if their driving force for insulating behavior is suppressed or overcome.

The rutile structure adopted by VO_2 for $T > 340$ K is of particular interest because its edge-sharing chains of octahedra are susceptible to the metal-metal dimerization characteristic of Peierls and Mott-Peierls MITs. In rutile structures, the d^0 electronic state on the metal atom yields a charge-transfer insulator with a p - d gap [Fig. 1(a)] while the d^1 electronic state can support a Peierls insulator in which the half-filled d_{xy} band splits into the filled $d_{||}$ band and the empty $d_{||}^*$ band [Fig. 1(b)] through metal-metal bonding. Several well-known MIT materials, VO_2 and NbO_2 [12,13], as well as computationally proposed MoON [14], all exhibit the rutile structure and the characteristic dimerization.

The trirutile structure ($A'A_2L_6$) is derived as an ordered cation substitutional phase of the rutile structure by substituting a different A' cation species for every third cation, which triples the unit cell along the c axis, illustrated in Fig. 1(c), while maintaining the tetragonal crystal system and two screw operations in the space group $P4_2/m2_1/n2/m$ (136) [15]. Notable trirutiles include $A'\text{Ta}_2\text{O}_6$ ($A' = \text{Ti}$ [16], Cr [17,18], Fe [18], Co [18–20], Ni [18,21,22], Cu [23], Zn [24]), $A'\text{Sb}_2\text{O}_6$ ($A' = \text{Cr}$ [16], Co [19,22,25], Cu [25]), $A'\text{Bi}_2\text{O}_6$ ($A' = \text{Mg}$, Zn) [26,27], WV_2O_6 [12,28], and TeMn_2O_6 [29]. While the cation pattern changes from $\dots A^{4+} - A^{4+} \dots$ to $\dots A^{5+} - A^{5+} - A'^{2+} \dots$, interrupting the quasi-1D chains and preventing a Peierls-like transition, this superstructure can still accommodate $A^{5+} - A^{5+}$ dimerization and induce an MIT for specific orbital fillings. Although MgTa_2O_6 with Ta^{5+} (d^0 electronic configuration) has been synthesized and characterized [18,24,30–35], its electronic structure has neither been extensively studied nor explored as a platform to realize MITs through electron doping (d^n , $n > 0$). Motivated by previous studies of carrier-driven MITs, e.g., La-doped SrTiO_3 [36], we examine the atomic and electronic structure of trirutile MgTa_2O_6 for electron-doping levels ranging from d^0 to d^1 . We find four electronic phases in MgTa_2O_6

^{*}kmliller@u.northwestern.edu[†]jrondinelli@northwestern.edu

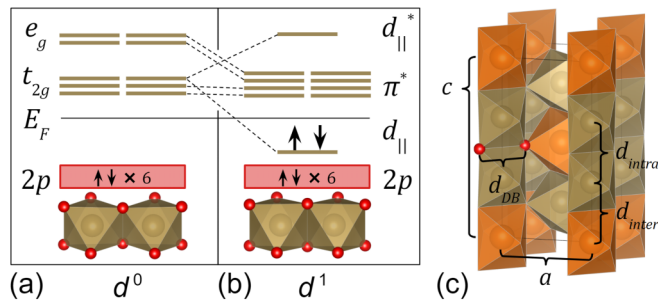


FIG. 1. Orbital diagrams for Ta-Ta pairs in (a) d^0 and (b) d^1 MgTa_2O_6 with Ta states in brown and oxygen states in red. (c) The crystal structure of MgTa_2O_6 with lattice parameters and important distances labeled: dimer-bridging oxygen-oxygen distance (d_{DB}), intradimer metal-metal distance (d_{intra}), and interdimer metal-metal distance (d_{inter}). Ligands located at octahedral vertices are omitted for clarity except the two oxygen ions (red spheres) located at the $4f$ site used to define d_{DB} .

across doping, draw parallels between the electronic and lattice properties of trirutile MgTa_2O_6 and those of rutile VO_2 , and comment on the effect of the distinct A' cation.

II. COMPUTATIONAL METHODS

We performed first-principles spin-polarized DFT calculations on MgTa_2O_6 using the Vienna *ab initio* Simulation Package (VASP) [37] with projector-augmented-wave pseudopotentials [38,39] within the Perdew-Burke-Ernzerhof generalized gradient approximation (PBE) [40]. Calculations including the Hubbard U correction used the method introduced by Dudarev *et al.* [41], which features U_{eff} as the only parameter. Electronic structures were further assessed using the Heyd-Scuseria-Ernzerhof (HSE06) hybrid range-separated functional that includes fractional Fock exchange [42]. We found no significant spin-orbit interaction effects, so the calculations presented here do not include spin-orbit interaction. Further details can be found in Sec. IV of the Supplemental Material [43]. For all calculations, we use a 800 eV plane-wave cutoff and treat the core and valence electrons with the following electronic configurations: $3s^2 3p^0$ (Mg), $5p^6 6s^1 5d^4$ (Ta), and $2s^2 2p^4$ (O). Ionic relaxations were performed in pristine structures (without electron doping) using an energy tolerance of 10^{-7} eV and a force tolerance of $1 \text{ meV } \text{\AA}^{-1}$. We sampled the Brillouin zone with a $6 \times 6 \times 3$ Γ -centered k -point mesh for MgTa_2O_6 and $6 \times 6 \times 9$ Γ -centered k -point mesh for TaO_2 , both corresponding to 1944 k points per reciprocal atom. We used the PHONOPY package with a $2 \times 2 \times 1$ supercell and 0.01 \AA displacements for pre- and postprocessing of the dynamical matrix [44]. We parsed and visualized our results with the PYTHON package PYMATGEN [45].

We simulated electron doping by modifying the number of excess electrons in MgTa_2O_6 using the NELECT tag in VASP. The resulting charge imbalance is automatically neutralized by a uniform background charge. However, this work-around introduces an unphysically large electronic pressure [46–49], which can cause spurious overexpansion of the unit cell under typical relaxation conditions. We avoid this issue by disal-

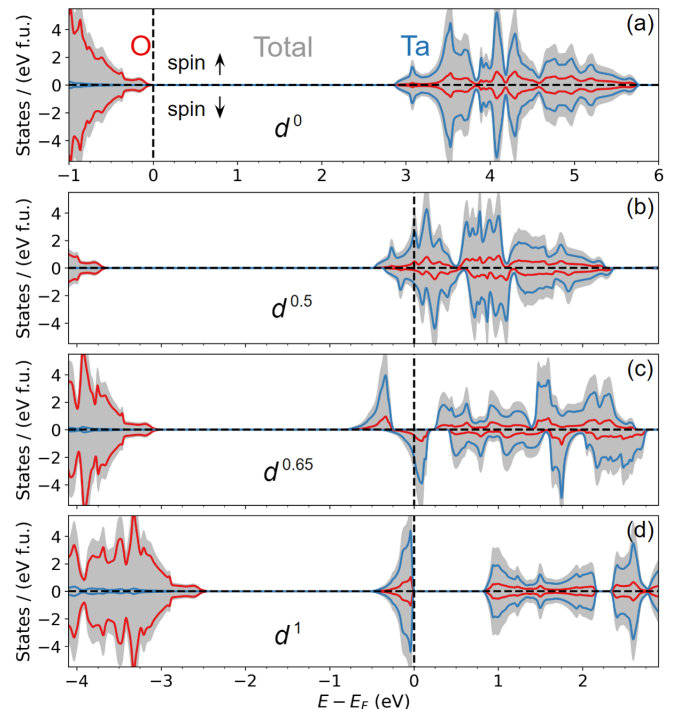


FIG. 2. Electronic density of states (DOS) of MgTa_2O_6 for electron concentrations (a) d^0 , (b) $d^{0.5}$, (c) $d^{0.65}$, and (d) d^1 . Magnesium does not significantly contribute to the DOS near the Fermi level.

lowing electron concentration-dependent cell expansion; the doped structures were obtained via fixed-volume relaxation from the relaxed undoped structures, allowing dimerization and evolution of the c/a ratio without spurious volume changes. Volume effects from electron doping are examined in further in Sec. I of the Supplemental Material [43].

III. RESULTS AND DISCUSSION

A. Carrier-induced electronic phases

Across the Ta d^0 to d^1 filling levels studied in MgTa_2O_6 , we identified four distinct phases distinguished by their electronic, magnetic, and lattice dynamical character. Figure 2 presents their electronic structures: nonmagnetic charge-transfer insulator, ferromagnetic metal, ferromagnetic half-metal, and nonmagnetic insulator. The pristine phase of MgTa_2O_6 is a d^0 charge-transfer insulator with a valence band composed of oxygen $2p$ states and a conduction band composed of tantalum $5d$ states with admixture of oxygen $2p$ states, as shown in the density of states in Fig. 2(a). The magnesium $2p$ states are only weakly hybridized with the oxygen bands, reflecting the ionic nature of the Mg-O interaction, and do not significantly contribute to the electronic structure near the Fermi level. Using the PBE functional, we calculated a band gap of approximately 3 eV. Compared to experimental measurements of 3.8 eV [50] and 4.34 eV [51], this gap is consistent with underestimation typical of semilocal DFT. Further analysis of electron correlation effects can be found in Sec. II of the Supplemental Material [43].

At electron concentrations less than $d^{0.5}$, the additional electrons cannot completely occupy an entire Ta $5d$ orbital

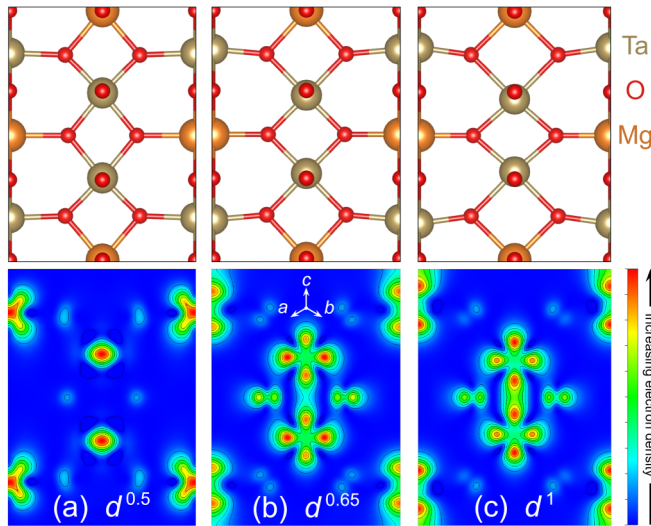


FIG. 3. Atomic structure and majority-spin valence band charge distributions of MgTa_2O_6 for electron concentrations of (a) $d^{0.5}$, (b) $d^{0.65}$, and (c) d^1 . Charge localization in the Ta-Ta dimer occurs with increasing electron concentration.

unless more than two Ta atoms per unit cell share the electrons. Since the trirutile structure does not permit bonding between more than two metal atoms, there is no driving force for d electron localization below $d^{0.5}$ filling. Instead, the d electrons are delocalized in the conduction band [Fig. 2(b)]. With insufficient electrons to occupy a single d orbital on each Ta-Ta pair, the electrons preferentially occupy one spin channel, making the phase a ferromagnetic metal with a spin moment that increases with both electron concentration and Hubbard U . Note that we tested all possible antiferromagnetic configurations compatible with $2 \times 2 \times 1$ and $1 \times 1 \times 2$ supercells, finding the ferromagnetic configuration to be the ground state.

At the $d^{0.5}$ concentration, we might expect a single electron to localize across each neighboring Ta-Ta pair, inducing a ferromagnetic half-metallic state. We find that this metal-to-half-metal transition boundary is functional dependent, occurring at an elevated level (near $d^{0.65}$) for PBE [Fig. 2(c)] and HSE06, but occurring at $d^{0.5}$ for PBE + U with $U_{\text{eff}} = 3$ eV (Fig. S2 [43]). In either case, this phase requires understanding electron distributions among the chains of edge-sharing octahedra along the c axis with periodic ordering of Ta-Ta-Mg cations, which we explore further below.

Upon increasing electron concentration, we encounter a critical level at which the potential energy for electrons localized in the Ta-Ta bond overcomes the kinetic energy for delocalizing the electrons across both spin channels. In response, one electron localizes in a $d_{||}$ orbital formed via hybridization of the d_{xy} orbitals of neighboring transition-metal atoms as in VO_2 and NbO_2 [2,13], opening a band gap in one spin channel. The other spin channel hosts the remaining 0.15 delocalized electrons per Ta, yielding a ferromagnetic half-metallic state [Fig. 2(c)]. The formation of the $d_{||}$ orbital in MgTa_2O_6 is discernible in slices of the valence band charge densities between Ta dimers (Fig. 3), which closely resemble

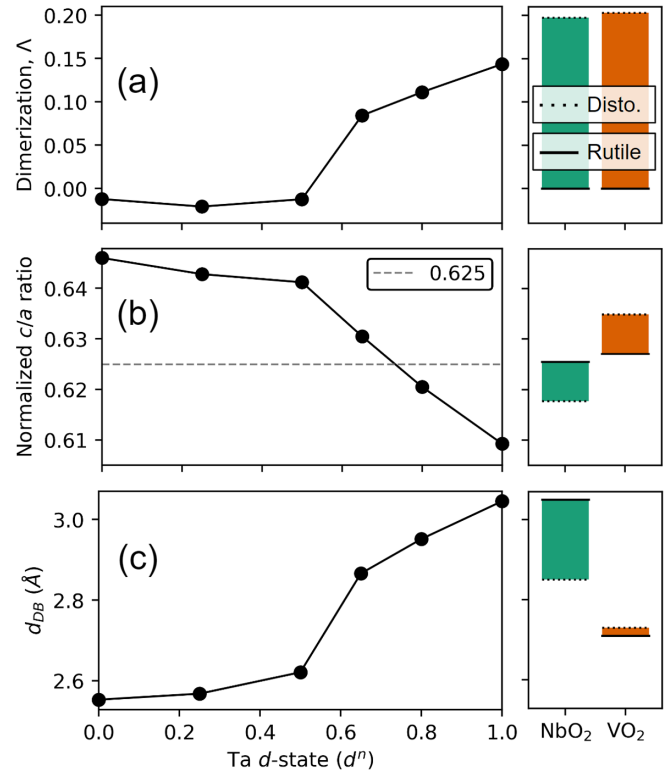


FIG. 4. Effect of electron concentration on (a) dimerization, (b) axial ratios, and (c) the dimer bridging oxygen-oxygen distance in MgTa_2O_6 . (right panels) Corresponding data for the rutile (solid line) and distorted (dotted line) phases of VO_2 [53] and NbO_2 [54] are shown on the same ordinate for comparison. The solid bars indicate the change in the structural parameter upon undergoing the phase transition. The axial ratio in the distorted structures is approximated using lattice constants and the following conversions from distorted (D) to rutile (R) structures: $\text{VO}_2(P2_1/c) \rightarrow c_R/a_R = \sqrt{a_D^2 + c_D^2 + 2a_Dc_D \cos \beta} / (2b_D)$ and $\text{NbO}_2(I4_1/a) \rightarrow c_R/a_R = c_D / (\sqrt{2}a_D)$.

the charge densities of NbO_2 presented by O'Hara and Demkov [52].

Upon increasing the electron concentration further, additional electrons localize across the dimer until the hybridization of neighboring d_{xy} bands forms a fully occupied singlet d state. The evolution in the d_{xy} orbital hybridization appears in Fig. 3 where the electron density between the Ta-Ta dimer increases drastically upon going from $d^{0.5} \rightarrow d^1$. The energy of the newly formed $d_{||}$ band shifts to lower energy and a band gap opens in both spin channels [Fig. 2(d) and illustrated in Figs. 1(a), 1(b)].

B. Carrier-induced changes in atomic structure

Compared to the archetypal rutile MIT materials, VO_2 and NbO_2 , MgTa_2O_6 exhibits similar structural changes across the MIT with a few key differences. Both trirutile and rutile compounds exhibit three MIT-related structure modifications: (i) dimerization, or shortening of the metal-metal distances across a shared octahedral edge, (ii) change in the c/a axial ratio, and (iii) elongation of the bridging oxygen distance of an octahedral edge across the transition. Figure 4 shows the

concentration dependence of these three structural features, which we describe further below, and their nonlinear dependence captures the onset of the carrier-induced MIT. Two key structural differences include (i) crystallographic symmetry reductions owing to the dimerization in rutile structures, and (ii) the antipolar zigzag distortion in the rutile structures are not found in trirutile structures such as n -type doped MgTa_2O_6 .

To compare dimerization between the rutile structure and the trirutile structures, we define a generalized dimerization as:

$$\Lambda = 2 \left(\frac{d_{\text{inter}} - d_{\text{intra}}}{d_{\text{inter}} + d_{\text{intra}}} \right),$$

where d_{inter} and d_{intra} indicate interdimer and intradimer metal-metal distances, respectively, as shown in Fig. 1(c). We find that dimerization increases across the transition in Fig. 4(a) especially between $d^{0.5}$ and $d^{0.65}$, confirming that the dimerization is directly coupled to the formation of the Ta-Ta bond and d_{\parallel} orbital. Furthermore, the extent of the dimerization in d^1 MgTa_2O_6 is close to that which occurs in the well-known d^1 rutile MIT materials NbO_2 and VO_2 [right panel, Fig. 4(a)]. We also note that $\Lambda < 0$ in our simulated trirutiles at low doping. This behavior means the Ta cations are further from each other than they are from the Mg cation owing to the poor electrostatic screening of the Ta-Ta repulsion at low d filling.

Another important structural indicator in rutile compounds is the axial (c/a) ratio. Hiroi proposed that the rutile structure features an inherent structural instability causing susceptibility to a structural transition (and concurrent MIT for some electron fillings) at a critical axial ratio near $c/a \sim 0.625$ [12]. The axial ratio can most easily be understood as a measure of the relative lengths of the bridging O-O (d_{DB}) and c -oriented M-M bonds (d_{inter} and d_{intra}) shown in Fig. 1(c), which compete owing to the herringbone connectivity pattern. Since the bridging O-O bond and the transverse M-M bond drive electron density, from O- p and M- d orbitals, respectively, into the same location in real space, strengthening one weakens the other. Furthermore, since the MIT in rutile oxides such as VO_2 and NbO_2 depends on the M-M dimerization along the c axis, the axial ratio sets the structural baseline upon which the MIT occurs. Hiroi's proposed critical axial ratio [12] thus represents a tipping point at which the coupled electronic and structural forces driving a dimerized, insulating state approximately balance those which drive a metallic state.

We compare the normalized axial ratio ($c/3a$) of trirutiles to the axial ratio (c/a) of rutiles to evaluate whether this inherent instability proposed for the rutile family has relevance in the trirutile family. Figure 4(b) shows that undoped MgTa_2O_6 features an axial ratio much larger than the critical value of 0.625, but as the electron concentration increases, the axial ratio decreases. The effect is weak at first because the additional electrons remain delocalized. Concurrent with the first electronic transition from metal to half-metal at $d^{0.65}$, the axial ratio decreases much faster with additional electrons, crossing the critical value near $d^{0.7}$. Comparing to Fig. 4(a), we note a similar trend in the dimerization values with little change until $d^{0.65}$. At this value, the dimerization rapidly increases to almost 10% and then continues to increase gradually to reach a maximum at the insulating d^1 state.

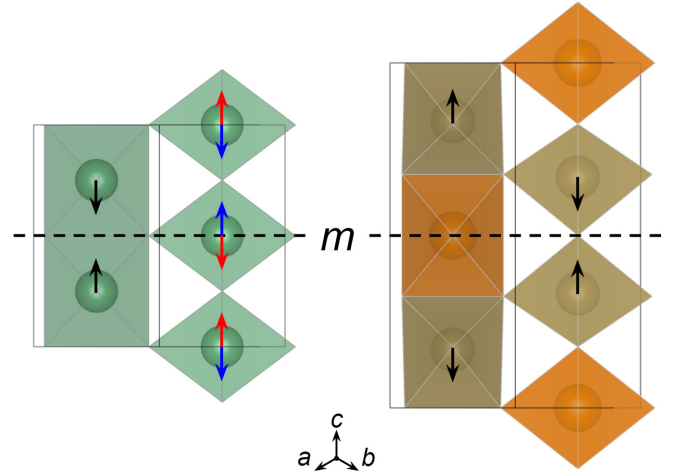


FIG. 5. The AL_2 rutile structure (left) cannot accommodate dimerization within the $P4/nmm$ space group due to the z -oriented mirror plane. The blue and red arrows show the two possible dimerization patterns compatible with the neighboring dimer, both of which lift the mirror operation. The $A'A_2L_6$ trirutile structure (right) preserves the mirror plane through A -site dimerization (black arrows). Ligands located at octahedral vertices are omitted for clarity.

Confirming the coupling between the lattice and the electronic transition in MgTa_2O_6 , we find that the bridging oxygen distance across the transition-metal dimer, d_{DB} , shown in Fig. 4(c), increases and follows the dimerization as MgTa_2O_6 is doped from a d^0 to d^1 insulator. This decrease in d_{DB} indicates that, like NbO_2 , MgTa_2O_6 features a removal of the bridging oxygen covalency via atomic separation as it approaches the insulating state [2,12]. Since this occurs in MgTa_2O_6 without a symmetry-breaking structural transition, we confirm the idea that this bridging oxygen repulsion is driven by the d_{\parallel} metal-metal bond formation. Furthermore, the clear inverse correlation between d_{DB} and the axial ratio in MgTa_2O_6 suggests that, as in NbO_2 , the decreasing axial ratio across the MIT is a result of the bridging oxygen separation (causing octahedral expansion in the ab plane) in concert with the expected Poisson contraction along the c direction. This structural picture is complicated in VO_2 where different structural trends occur; the axial ratio increases across the transition with very little change in d_{DB} . These inconsistencies are likely due to the zigzag V displacements (see Fig. 6) and the stronger role of electron correlation in its MIT.

Despite the similarity of the dimerization between the rutile and trirutile structures, the existence of additional Wyckoff sites in the trirutile structure eliminates the symmetry-breaking requirement. Table I shows that the rutile structure (AL_2) contains a single Wyckoff site each for the metal (A) and ligand (L) species, whereas the trirutile structure ($A'A_2L_6$) possesses two Wyckoff sites each for the metal (A' , A) and ligand (L) species. For dimerization to occur, the metal site must not only be free to move in the z direction but also antiparallel to its edge-connected neighbors. With only a single Wyckoff site, the rutile structure cannot dimerize as observed in the insulating phases of VO_2 and NbO_2 without reducing its $P4_2/nmm$ symmetry. Figure 5 illustrates this constraint in a doubled rutile unit cell, the black arrows show the

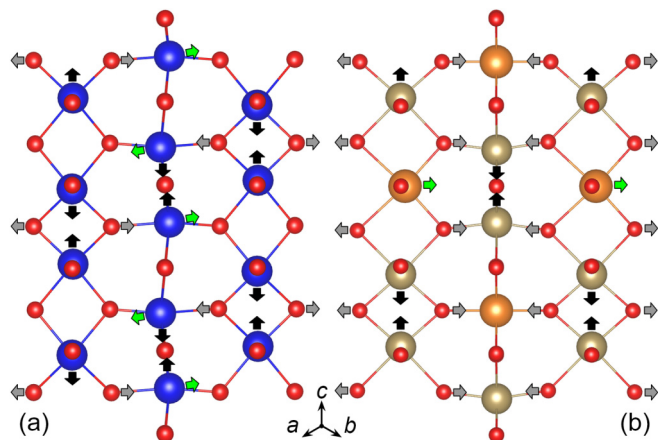


FIG. 6. Comparison of the lattice distortion across the MITs in (a) VO_2 and (b) $d^1 \text{MgTa}_2\text{O}_6$. Black arrows indicate dimerization, green arrows indicate zigzag distortion, and gray arrows indicate bridging oxygen separation. Note that the zigzag distortion (green arrows) in MgTa_2O_6 is predicted to occur only if the doped structure exceeds a critical volume.

dimerization pattern of the left-hand chain while the red and blue arrows show two possible dimerization patterns for the neighboring chain. However, both red and blue dimerization patterns remove the mirror plane with a normal axis along z in $P4_2/mnm$ (horizontal dashed line), indicating that the rutile structure must lower its symmetry (at a minimum from $P4_2/mnm$ to $P\bar{4}2_1m$) to accommodate dimerization. In the case of the trirutile unit cell, the intervening A' atom changes the neighbor-chain offset such that interchain neighbors do not coincide in the ab plane. This lack of overlap means that the mirror plane bisecting any given dimer does not intersect with dimers in neighboring chains. Rather the mirror plane bisects the A' atom, which is located at the midpoint between intrachain dimer neighbors, thereby preserving the mirror operation across any dimerization. As a result, the dimerization pattern in trirutiles ($A'-A-A$) differs from that found in rutiles ($A-A$). This trirutile dimerization maintains Peierls-like character if the intervening A' cation is electronically inactive (here, Mg^{2+}).

The ability of the trirutile structure to undergo dimerization without breaking the $P4_2/mnm$ results from the nonsymmorphic symmetries producing the neighbor-chain offset of the transition-metal pairs along the edge-sharing chains. We gen-

eralize this relationship to all superstructural variants with paired A sites, grouping them by their c -chain motif into those with symmetry-preserving dimerization: $[A'-]^{2n+1}A-A-$ and those with symmetry-breaking dimerization: $[A'-]^{2n}A-A-$, for $n \in \mathbb{Z} \geq 0$. The pattern dependence of this isosymmetric dimerization ability warrants further study of the other Magnéli-like superstructures of the rutile structure, e.g., cation patterns such as $A'-A-$, $A'-A'-A-A-$, $A'-A-A-A-$, etc.

Beyond the structural indicators derived from cooperative displacements, we further compare the displacive components of the MIT in MgTa_2O_6 to those of VO_2 , revealing the second key difference between the two structures. In VO_2 , the MIT is accompanied by two structural distortions: dimerization of V cations within the edge-sharing chains of VO_6 octahedra and an antipolar zigzag distortion [2], as shown in Fig. 6(a). The dimerization and zigzag distortions cooperatively stabilize the bonding $d_{||}$ orbital and destabilize the antibonding π^* state, respectively [12,55]. As seen in Fig. 6, the zigzag distortion produces further V off centering in the direction perpendicular to the V-V chains. Not only does this off centering destabilize π^* states by reducing overlap between $V-d_{x^2-y^2}$ and $O-p_{x/y}$ orbitals, it also allows the bridging oxygen atoms of neighboring chains to displace further apart, thereby further reducing the overlap of the bridging oxygen p orbitals. This reduced overlap allows for enhanced dimerization of the V^{4+} cations [Fig. 6(a)], and therefore further stabilizes the $d_{||}$ band [12]. Although the dimerization bears direct responsibility for splitting the d_{xy} band, current evidence points to the cooperative zigzag distortion being necessary for the full occupation of the $d_{||}$ orbital and therefore the MIT [2,55].

For contrast, MgTa_2O_6 requires no zigzag distortion to achieve an insulating state [Fig. 6(b)]. In Fig. S3 [43], we show the phonon spectrum in the (001) plane for four representative electron concentrations. We find in all phases except the FM half-metallic phase, the structure is dynamically stable. The instability calculated in the $d^{0.65}$ system is not a zigzag distortion but instead resembles the $M2$ phase of VO_2 , with dimerization and full singlet-state formation occurring in only half of the edge-sharing chains. While this indicates that $M2$ -like phases can exist in trirutiles, we found the lattice distortion to be favorable at only very small amplitudes and offer very little energy decrease to the system (about 4 meV/atom). The key difference between $d^1 \text{MgTa}_2\text{O}_6$ and VO_2 is the absence of an unstable zigzag mode in the phonons. Although VO_2 requires the zigzag displacements to fully open the band gap, $d^1 \text{MgTa}_2\text{O}_6$ requires no such distortion, instead achieving an insulating state within tetragonal $P4_2/mnm$ symmetry.

TABLE I. Comparison of the occupied metal (A' and A) and ligand (L) sites in the rutile and trirutile structures. The reduced x and z coordinates indicate free positions.

Structure	Atom	Site	Symmetry	Coordinates
Rutile	A	$2a$	$m.mm$	$(0, 0, 0)$
	L	$4f$	$m.2m$	$(x, x, 0)$
	A'	$2a$	$m.mm$	$(0, 0, 0)$
Trirutile	A	$4e$	$2.mm$	$(0, 0, z_M)$
	L	$4f$	$m.2m$	$(x_1, x_1, 0)$
	L	$8j$	$.m$	(x_2, x_2, z_L)

C. Accessing the electronic phases

We propose several strategies, such as chemical doping, photodoping, and strain, to access the aforementioned carrier-controlled phases. A' -site substitution, anion substitution, and oxygen vacancies all have the potential to increase the electron concentration in MgTa_2O_6 . Examples of such doping in rutiles include tungsten doping in VO_2 [56], titanium doping in NbO_2 [57], nitrogen doping in MoO_2 [14], and oxygen vacancies in TiO_2 [58]. In trirutiles, substitution of trivalent cations such as Al^{3+} , Fe^{3+} , Mn^{3+} , Sc^{3+} , Yb^{3+} , and Ga^{3+} for

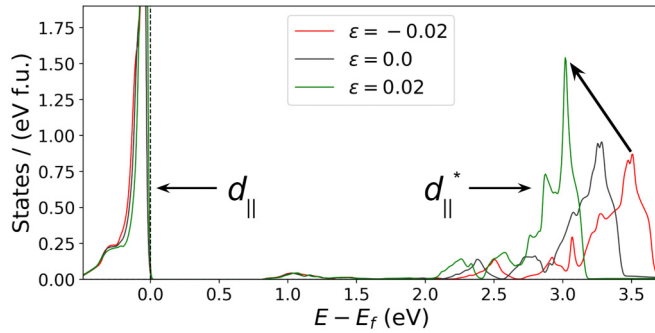


FIG. 7. Electronic DOS projected on the d_{\parallel} orbitals for three levels of uniaxial tensile strain (ϵ) along the c axis for d^1 MgTa_2O_6 . The black arrow indicates the shift in orbital states upon going from compressive ($\epsilon < 0$) to tensile ($\epsilon > 0$) strain.

Mg^{2+} could contribute a free electron to the conduction band states provided these dopants are shallow donors. Similarly, substitution of monovalent anions such as F^- , Cl^- , Br^- , and I^- for oxygen and oxygen vacancies could further contribute one and two free electrons per defect, respectively. Atomic simulations by Tealdi *et al.* predict that A' -site doping will be difficult to achieve in MgTa_2O_6 since trivalent cations prefer to occupy the A site [59]. Oxygen vacancies, on the other hand, have already been observed in MgTa_2O_6 [60]. However, Tealdi *et al.* predict that the $4f$ oxygen sites [those spanning d_{DB} in Fig. 1(c)], are the most favorable vacancy site [59]. The effect of such vacancies on dimerization in trirutiles is an open question and left for future work. Photodoping may be used either alone or in conjunction with chemical doping to access the three phases in MgTa_2O_6 , because it has been used to trigger and explore the MIT in VO_2 [61–64].

Beyond controlling the electron concentration, mechanical strain provides a route to change energies of certain electronic bands and thereby exert finer control over electronic properties. Strain effects are important not only as a response of a thin film deposited heteroepitaxially on a substrate, but a demonstrated strategy to tune the energy and bandwidths of the d_{\parallel} bands and the metal-insulator transition temperature in VO_2 [65–68]. Figure 7 shows the bonding d_{\parallel} orbital below the Fermi level and the antibonding d_{\parallel}^* orbital between 2 and 4 eV. Despite the intervening Mg atom in the octahedral chains, trirutile MgTa_2O_6 exhibits similar strain-dependent changes in its electronic structure found in VO_2 [66]. The d_{\parallel}^* orbital is stabilized by uniaxial tensile strain and destabilized by compressive strain relative to the bonding d_{\parallel} orbitals. This similarity indicates that the MIT behavior persists through small strains in trirutile oxides as in rutile oxides, opening avenues for similar thin film applications. More details about strain at different electron concentrations can be found in Sec. V of the Supplemental Material [43].

D. A' -site effects

Given that the trirutile structure is a superstructural variant of rutile, the only fundamental difference between TaO_2 and MgTa_2O_6 is the Mg on the new A' -site position. In addition to enabling symmetry-preserving dimerization as discussed in Sec. III. B, the most notable effect of the intervening Mg

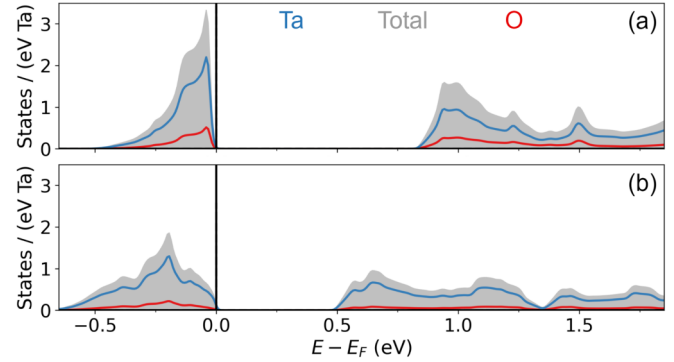


FIG. 8. Comparison of the electronic DOS for (a) d^1 MgTa_2O_6 and (b) rutile TaO_2 upon enforcing a dimerization of similar magnitude to that present in d^1 MgTa_2O_6 .

atoms is the confinement of the d_{\parallel} band. In Fig. 8, we find that the d_{\parallel} (valence) bandwidth shrinks from ≈ 0.7 eV to ≈ 0.4 eV upon making the ordered Mg_{Ta} substitution that converts rutile TaO_2 to trirutile MgTa_2O_6 . This confinement effect can be attributed to the loss of the long Ta-Ta interaction, which is present in the A - A dimerization pattern but missing from the A' - A - A pattern in trirutile. We can qualitatively frame this effect as the result of restricting electron hopping between neighboring Ta atoms. From TaO_2 to MgTa_2O_6 , the maximum Ta-Ta distance along the quasi-1D chains increases from 2.89 Å to 3.87 Å.

IV. CONCLUSION

We described the electronic, structural, and lattice dynamical behavior across electron doping in MgTa_2O_6 , spanning the continuum between the simple d^0 charge-transfer insulator and the d^1 dimerized insulator. We drew parallels between the MIT in trirutile MgTa_2O_6 and those that occur in the well-studied rutile oxides VO_2 and NbO_2 . We focused on the changes in dimerization along the c axis, formation of a d_{\parallel} orbital from neighboring transition-metal d_{xy} states, axial ratio near 0.625, suppression of bridging oxygen covalency across the MIT, and d_{\parallel}^* tuning via uniaxial strain. We also highlighted several differences between the rutile and trirutile structures, most notably symmetry-preserving dimerization in trirutiles, the absence of a concurrent zigzag distortion, and (contrasting VO_2) the minimal role of electron correlation in the opening of the band gap in MgTa_2O_6 . We propose that trirutile oxides and other superstructural variants of rutile oxides show promise as a new materials prototype from which to design MITs with greater chemical flexibility. We suggest strain, chemical doping, and photodoping as methods for accessing the rich electronic phase space of MgTa_2O_6 and other trirutiles.

ACKNOWLEDGMENTS

We thank Prof. Ram Seshadri, Prof. Stephen Wilson, Dr. Emily Schueller, and Julia Zuo of the University of California, Santa Barbara, for their fruitful discussions. This work was supported in part by the National Science Foundation (NSF) under Awards No. DMR-1729303 and No. DGE-1842165. Calculations were performed on the Extreme

Science and Engineering Discovery Environment (XSEDE), which is supported by NSF (ACI-1548562). This research was also supported in part through the computational resources and staff contributions provided for the Quest

high-performance computing facility at Northwestern University which is jointly supported by the Office of the Provost, the Office for Research, and Northwestern University Information Technology.

- [1] M. Imada, A. Fujimori, and Y. Tokura, Metal-insulator transitions, *Rev. Mod. Phys.* **70**, 1039 (1998).
- [2] J. B. Goodenough, The two components of the crystallographic transition in VO₂, *J. Solid State Chem.* **3**, 490 (1971).
- [3] J. Orenstein, Advances in the physics of high-temperature superconductivity, *Science* **288**, 468 (2000).
- [4] Y. Yanase, T. Jujo, T. Nomura, H. Ikeda, T. Hotta, and K. Yamada, Theory of superconductivity in strongly correlated electron systems, *Phys. Rep.* **387**, 1 (2003).
- [5] E. Dagotto, Complexity in strongly correlated electronic systems, *Science* **309**, 257 (2005).
- [6] H. Takagi and H. Y. Hwang, An emergent change of phase for electronics, *Science* **327**, 1601 (2010).
- [7] D. M. Newns, J. A. Misewich, C. C. Tsuei, A. Gupta, B. A. Scott, and A. Schrott, Mott transition field effect transistor, *Appl. Phys. Lett.* **73**, 780 (1998).
- [8] S. Hormoz and S. Ramanathan, Limits on vanadium oxide Mott metal-insulator transition field-effect transistors, *Solid-State Electron.* **54**, 654 (2010).
- [9] N. Shukla, A. V. Thathachary, A. Agrawal, H. Paik, A. Aziz, D. G. Schlom, S. K. Gupta, R. Engel-Herbert, and S. Datta, A steep-slope transistor based on abrupt electronic phase transition, *Nature Commun.* **6**, 7812 (2015).
- [10] S. Kabir, S. Nirantar, L. Zhu, C. Ton-That, S. K. Jain, A. B. A. Kayani, B. J. Murdoch, S. Sriram, S. Walia, and M. Bhaskaran, Phase change vanadium dioxide light sensors, *Appl. Mater. Tod.* **21**, 100833 (2020).
- [11] S. Kumar, R. S. Williams, and Z. Wang, Third-order nanocircuit elements for neuromorphic engineering, *Nature (London)* **585**, 518 (2020).
- [12] Z. Hiroi, Structural instability of the rutile compounds and its relevance to the metal-insulator transition of VO₂, *Prog. Solid State Chem.* **43**, 47 (2015).
- [13] V. Eyert, The metal-insulator transition of NbO₂: An embedded Peierls instability, *Europhys. Lett.* **58**, 851 (2002).
- [14] N. J. Szymanski, L. N. Walters, D. Puggioni, and J. M. Rondinelli, Design of Heteroanionic MoON Exhibiting a Peierls Metal-Insulator Transition, *Phys. Rev. Lett.* **123**, 236402 (2019).
- [15] Rutile type derivatives, *Z. Kristallogr. - Cryst. Mater.* **209**, 143 (1994).
- [16] E. C. Schueller, Y. M. Oey, K. D. Miller, K. E. Wyckoff, R. Zhang, W. Zhang, S. D. Wilson, J. M. Rondinelli, and R. Seshadri, AB₂X₆ compounds and the stabilization of trirutile oxides, *Inorg. Chem.* **60**, 9224 (2021).
- [17] M. Saes, N. Raju, and J. Greedan, Structure and magnetism in CrTa₂O₆: A trirutile oxide based on Cr₂₊, *J. Solid State Chem.* **140**, 7 (1998).
- [18] A. Gupta, P. Singh, H. Celio, C. B. Mullins, and J. B. Goodenough, Conditions for Ta^{IV}-Ta^{IV} bonding in trirutile Li_{1-x}M_xTa₂O₆, *Inorg. Chem.* **54**, 2009 (2015).
- [19] J. Reimers, J. Greedan, C. Stager, and R. Kremer, Crystal structure and magnetism in CoSb₂O₆ and CoTa₂O₆, *J. Solid State Chem.* **83**, 20 (1989).
- [20] E. Kinast, C. dos Santos, D. Schmitt, O. Isnard, M. Gusmão, and J. da Cunha, Magnetic structure of the quasi-two-dimensional compound CoTa₂O₆, *J. Alloys Compd.* **491**, 41 (2010).
- [21] J. M. Law, H.-J. Koo, M.-H. Whangbo, E. Brücher, V. Pomjakushin, and R. K. Kremer, Strongly correlated one-dimensional magnetic behavior of NiTa₂O₆, *Phys. Rev. B* **89**, 014423 (2014).
- [22] A. B. Christian, S. H. Masunaga, A. T. Schye, A. Rebello, J. J. Neumeier, and Y.-K. Yu, Magnetic field influence on the Néel, dimer, and spin-liquid states of the low-dimensional anti-ferromagnets NiTa₂O₆ and CoSb₂O₆, *Phys. Rev. B* **90**, 224423 (2014).
- [23] A. Golubev, R. E. Dinnebier, A. Schulz, R. K. Kremer, H. Langbein, A. Senyshyn, J. M. Law, T. C. Hansen, H.-J. Koo, and M.-H. Whangbo, Structural and magnetic properties of the trirutile-type 1D-Heisenberg anti-ferromagnet CuTa₂O₆, *Inorg. Chem.* **56**, 6318 (2017).
- [24] C. Ferrari and A. Hernandez, MgTa₂O₆ and ZnTa₂O₆ ceramics from oxide precursors, *J. Eur. Ceram. Soc.* **22**, 2101 (2002).
- [25] D. T. Maimone, A. B. Christian, J. J. Neumeier, and E. Granado, Lattice dynamics of ASb₂O₆ (A = Cu, Co) with trirutile structure, *Phys. Rev. B* **97**, 104304 (2018).
- [26] N. Kumada, N. Takahashi, N. Kinomura, and A. W. Sleight, Preparation of ABi₂O₆ (A = Mg, Zn) with the trirutile-type structure, *Mater. Res. Bull.* **32**, 1003 (1997).
- [27] M. A. Rahman, M. A. Rahman, U. K. Chowdhury, M. Bhuiyan, M. L. Ali, and M. A. R. Sarker, First principles investigation of structural, elastic, electronic and optical properties of ABi₂O₆ (A = Mg, Zn) with trirutile-type structure, *Cogent Physics* **3**, 1257414 (2016).
- [28] G. Pourroy, M. Drillon, L. Padel, and J. C. Bernier, The orbitally degenerate binuclear unit $t^2_{2g} - t^2_{2g}$: Part II: Interaction between vanadium III ions in the WV₂O₆ compound, *Physica B+C* **123**, 21 (1983).
- [29] N. Matsubara, F. Damay, B. Vertruyen, N. Barrier, O. I. Lebedev, P. Boullay, E. Elkaïm, P. Manuel, D. D. Khalyavin, and C. Martin, Mn₂TeO₆: A distorted inverse trirutile structure, *Inorg. Chem.* **56**, 9742 (2017).
- [30] H.-J. Lee, I.-T. Kim, and K. S. Hong, Dielectric properties of AB₂O₆ compounds at microwave frequencies (A = Ca, Mg, Mn, Co, Ni, Zn, and B = Nb, Ta), *Jpn. J. Appl. Phys.* **36**, L1318 (1997).
- [31] H. Wu, Y. Jiang, and Y. Yue, Low-temperature synthesis and microwave dielectric properties of trirutile-structure MgTa₂O₆ ceramics by aqueous sol-gel process, *Ceram. Int.* **38**, 5151 (2012).
- [32] J.-M. Wu, I. Djerdj, T. von Graberg, and B. M. Smarsly, Mesoporous MgTa₂O₆ thin films with enhanced photocatalytic

- activity: On the interplay between crystallinity and mesostructure, *Beilstein J. Nanotechnol.* **3**, 123 (2012).
- [33] D. Sun, S. Senz, and D. Hesse, Topotaxial formation of $\text{Mg}_4\text{Ta}_2\text{O}_9$ and MgTa_2O_6 thin films by vapour-solid reactions on MgO (001) crystals, *J. Eur. Ceram. Soc.* **24**, 2453 (2004).
- [34] T. Liu, M. Dupuis, and C. Li, Band structure engineering: insights from defects, band gap, and electron mobility, from study of magnesium tantalate, *J. Phys. Chem. C* **120**, 6930 (2016).
- [35] R. Baral, H. S. Fierro, C. Rueda, B. Sahu, A. M. Strydom, N. Poudel, K. Gofryk, F. S. Manciu, C. Ritter, T. W. Heitmann, B. P. Belbase, S. Bati, M. P. Ghimire, and H. S. Nair, Signatures of low-dimensional magnetism and short-range magnetic order in Co-based trirutiles, *Phys. Rev. B* **100**, 184407 (2019).
- [36] O. A. Marina, N. L. Canfield, and J. W. Stevenson, Thermal, electrical, and electrocatalytic properties of lanthanum-doped strontium titanate, *Solid State Ionics* **149**, 21 (2002).
- [37] G. Kresse and J. Furthmüller, Efficient iterative schemes for ab initio total-energy calculations using a plane-wave basis set, *Phys. Rev. B* **54**, 11169 (1996).
- [38] P. E. Blöchl, Projector augmented-wave method, *Phys. Rev. B* **50**, 17953 (1994).
- [39] G. Kresse and D. Joubert, From ultrasoft pseudopotentials to the projector augmented-wave method, *Phys. Rev. B* **59**, 1758 (1999).
- [40] J. P. Perdew, K. Burke, and M. Ernzerhof, Generalized Gradient Approximation Made Simple, *Phys. Rev. Lett.* **77**, 3865 (1996).
- [41] S. L. Dudarev, G. A. Botton, S. Y. Savrasov, C. J. Humphreys, and A. P. Sutton, Electron-energy-loss spectra and the structural stability of nickel oxide: An LSDA + U study, *Phys. Rev. B* **57**, 1505 (1998).
- [42] J. Heyd, G. E. Scuseria, and M. Ernzerhof, Hybrid functionals based on a screened Coulomb potential, *J. Chem. Phys.* **118**, 8207 (2003).
- [43] See Supplemental Material at <http://link.aps.org/supplemental/10.1103/PhysRevMaterials.6.075007> for additional computational details including volume effects, lattice dynamical properties, electron correlation, and spin-orbit coupling effects. It also includes Refs. [69–71] not cited in the main text.
- [44] A. Togo and I. Tanaka, First principles phonon calculations in materials science, *Scr. Mater.* **108**, 1 (2015).
- [45] S. P. Ong, W. D. Richards, A. Jain, G. Hautier, M. Kocher, S. Cholia, D. Gunter, V. L. Chevrier, K. A. Persson, and G. Ceder, Python materials genomics (pymatgen): A robust, open-source python library for materials analysis, *Comput. Mater. Sci.* **68**, 314 (2013).
- [46] Y. Iwazaki, T. Suzuki, Y. Mizuno, and S. Tsuneyuki, Doping-induced phase transitions in ferroelectric BaTiO_3 from first-principles calculations, *Phys. Rev. B* **86**, 214103 (2012).
- [47] F. Bruneval, C. Varvenne, J.-P. Crocombette, and E. Clouet, Pressure, relaxation volume, and elastic interactions in charged simulation cells, *Phys. Rev. B* **91**, 024107 (2015).
- [48] V. F. Michel, T. Esswein, and N. A. Spaldin, Interplay between ferroelectricity and metallicity in BaTiO_3 , *J. Mater. Chem. C* **9**, 8640 (2021).
- [49] D. Hickox-Young, D. Puggioni, and J. M. Rondinelli, Persistent polar distortions from covalent interactions in doped BaTiO_3 , *Phys. Rev. B* **102**, 014108 (2020).
- [50] M. Birdeanu, M. Vaida, and E. Fagadar-Cosma, Hydrothermal synthesis of ZnTa_2O_6 , ZnNb_2O_6 , MgTa_2O_6 and MgNb_2O_6 pseudo-binary oxide nanomaterials with anticorrosive properties, *Manuf. Rev.* **7**, 39 (2020).
- [51] S. Chen, Y. Qi, G. Liu, J. Yang, F. Zhang, and C. Li, A wide visible-light-responsive tunneled $\text{MgTa}_2\text{O}_{6-x}\text{N}_x$ photocatalyst for water oxidation and reduction, *Chem. Commun.* **50**, 14415 (2014).
- [52] A. O'Hara and A. A. Demkov, Nature of the metal-insulator transition in NbO_2 , *Phys. Rev. B* **91**, 094305 (2015).
- [53] K. D. Rogers, An x-ray diffraction study of semiconductor and metallic vanadium dioxide, *Powder Diffr.* **8**, 240 (1993).
- [54] A. A. Bolzan, C. Fong, B. J. Kennedy, and C. J. Howard, A powder neutron diffraction study of semiconducting and metallic niobium dioxide, *J. Solid State Chem.* **113**, 9 (1994).
- [55] M. W. Haverkort, Z. Hu, A. Tanaka, W. Reichelt, S. V. Streltsov, M. A. Korotin, V. I. Anisimov, H. H. Hsieh, H.-J. Lin, C. T. Chen, D. I. Khomskii, and L. H. Tjeng, Orbital-Assisted Metal-Insulator Transition in VO_2 , *Phys. Rev. Lett.* **95**, 196404 (2005).
- [56] X. Tan, T. Yao, R. Long, Z. Sun, Y. Feng, H. Cheng, X. Yuan, W. Zhang, Q. Liu, C. Wu, Y. Xie, and S. Wei, Unraveling metal-insulator transition mechanism of VO_2 triggered by tungsten doping, *Sci. Rep.* **2**, 466 (2012).
- [57] D. S. Jeon, T. D. Dongale, and T. G. Kim, Low power Ti-doped NbO_2 -based selector device with high selectivity and low OFF current, *J. Alloys Compd.* **884**, 161041 (2021).
- [58] R. Schaub, P. Thosttrup, N. Lopez, E. Lægsgaard, I. Stensgaard, J. K. Nørskov, and F. Besenbacher, Oxygen Vacancies as Active Sites for Water Dissociation on Rutile TiO_2 (110), *Phys. Rev. Lett.* **87**, 266104 (2001).
- [59] C. Tealdi, M. Saiful Islam, L. Malavasi, and G. Flor, Defect and dopant properties of MgTa_2O_6 , *J. Solid State Chem.* **177**, 4359 (2004).
- [60] D. Xu, S. Gao, W. Liu, Y. Liu, Q. Zhou, L. Li, T. Cui, and H. Yuan, The Raman scattering of trirutile structure MgTa_2O_6 single crystals grown by the optical floating zone method, *RSC Adv.* **9**, 839 (2019).
- [61] A. Cavalleri, T. Dekorsy, H. H. W. Chong, J. C. Kieffer, and R. W. Schoenlein, Evidence for a structurally-driven insulator-to-metal transition in VO_2 : A view from the ultrafast timescale, *Phys. Rev. B* **70**, 161102(R) (2004).
- [62] M. Rini, Z. Hao, R. W. Schoenlein, C. Giannetti, F. Parmigiani, S. Fourmaux, J. C. Kieffer, A. Fujimori, M. Onoda, S. Wall, and A. Cavalleri, Optical switching in VO_2 films by below-gap excitation, *Appl. Phys. Lett.* **92**, 181904 (2008).
- [63] H. Dachraoui, N. Müller, G. Obermeier, C. Oberer, S. Horn, and U. Heinzmann, Interplay between electronic correlations and coherent structural dynamics during the monoclinic insulator-to-rutile metal phase transition in VO_2 , *J. Phys.: Condens. Matter* **23**, 435402 (2011).
- [64] S. Wall, S. Yang, L. Vidas, M. Chollet, J. M. Glowia, M. Kozina, T. Katayama, T. Henighan, M. Jiang, T. A. Miller, D. A. Reis, L. A. Boatner, O. Delaire, and M. Trigo, Ultrafast disordering of vanadium dimers in photoexcited VO_2 , *Science* **362**, 572 (2018).
- [65] B. Lazarovits, K. Kim, K. Haule, and G. Kotliar, Effects of strain on the electronic structure of VO_2 , *Phys. Rev. B* **81**, 115117 (2010).

- [66] J. Laverock, L. F. J. Piper, A. R. H. Preston, B. Chen, J. McNulty, K. E. Smith, S. Kittiwatanakul, J. W. Lu, S. A. Wolf, P.-A. Glans, and J.-H. Guo, Strain dependence of bonding and hybridization across the metal-insulator transition of VO₂, *Phys. Rev. B* **85**, 081104(R) (2012).
- [67] S. Kittiwatanakul, S. A. Wolf, and J. Lu, Large epitaxial bi-axial strain induces a Mott-like phase transition in VO₂, *Appl. Phys. Lett.* **105**, 073112 (2014).
- [68] W.-C. Lee, M. J. Wahila, S. Mukherjee, C. N. Singh, T. Eustance, A. Regoutz, H. Paik, J. E. Boschker, F. Rodolakis, T.-L. Lee, D. G. Schlom, and L. F. J. Piper, Cooperative effects of strain and electron correlation in epitaxial VO₂ and NbO₂, *J. Appl. Phys.* **125**, 082539 (2019).
- [69] R. M. Wentzcovitch, W. W. Schulz, and P. B. Allen, VO₂: Peierls or Mott-Hubbard? A view from band theory, *Phys. Rev. Lett.* **72**, 3389 (1994).
- [70] Z. Zhu and U. Schwingenschlögl, Comprehensive picture of VO₂ from band theory, *Phys. Rev. B* **86**, 075149 (2012).
- [71] S. Kim, K. Kim, C.-J. Kang, and B. I. Min, Correlation-assisted phonon softening and the orbital-selective Peierls transition in VO₂, *Phys. Rev. B* **87**, 195106 (2013).